American Mineralogist, Volume 79, pages 654–667, 1994

TEM study of relationships between the microstructures and magnetic properties of strongly magnetized magnetite and maghemite

Jillian F. Banfield
Department of Geology and Geophysics, University of Wisconsin–Madison, Madison, Wisconsin 53706, U.S.A.
Peter J. Wasilewski
Laboratory for Extraterrestrial Physics, NASA–Goddard Space Flight Center, Code 691, Greenbelt, Maryland 20771, U.S.A.
David R. Veblen
Department of Earth and Planetary Sciences, Johns Hopkins University, Baltimore, Maryland 21218, U.S.A.

Abstract

This study investigates relationships between microstructures revealed by transmission electron microscopy (TEM) and the magnetic properties of strongly magnetized magnetite iron ore previously described as type I lodestone. The sample consists mostly of magnetite with some maghemite (~30%) and minor hematite and goethite oxidation products (<5%). The maghemite exhibits a weakly developed superstructure that in some areas is consistent with the enantiomorphous space groups $P4_132$ and $P4_332$. High-resolution imaging indicates that magnetite and maghemite contain closely spaced planar faults parallel to {101}. Displacement vector analyses and high-resolution imaging indicate ⟨¼¼0⟩ translations across most faults. Faults cannot arise merely by oxidation and vacancy ordering because they offset the magnetite substructure. Boundaries that show no offset of the magnetite substructure probably represent junctions between enantiomorphous maghemite domains. Although superlattices are not sufficiently well developed to allow detailed characterization of the vacancy ordering patterns, we can establish that the ⟨¼¼0⟩ boundaries generally separate regions of the same phase and not regions of magnetite from maghemite. Needle-shaped areas defined by planar faults are elongate along the magnetically soft [111] direction, and defect orientations correspond to the usual orientations of magnetic domain walls in magnetite. As noted previously, Fe-O-Fe bond angles across {101} faults allow direct reversal of the magnetic moments. Modification of magnetic vector orientations would require either nucleation of new domain walls or the movement of faults.

Three specific thermal regimes (20–280, 280–425, and 425–600 °C) are derived from a series of thermomagnetic experiments; each regime is associated with the movement of the natural remanent magnetization (NRM) vector. The ratio of NRM to saturation remanent magnetization is large, consistent with lightning-discharge induced magnetization. In the first regime, 80% of the NRM is destroyed, the coercivity is substantially reduced, and the magnetic susceptibility increases. These changes correlate with the elimination of most stacking faults from the sample. We suggest that the initial high coercivity is directly associated with the presence of stacking faults and that pinning of domain walls by these features primarily explains the large and stable natural remanence. The shape anisotropy of the magnetite and maghemite regions may also be important. We tentatively suggest that the stacking faults may also have been induced in the lightning event. The second thermal regime, characterized by rapid reduction in susceptibility and saturation magnetization, corresponds to the conversion of maghemite to hematite. The third regime is dominated by magnetite and hematite. Results demonstrate that microstructural detail revealed by TEM contributes substantially to the understanding of mineral magnetic properties.

Introduction

Since the earliest studies of rock magnetism (see, for example, Nagata, 1961; Uyeda, 1958; Graham, 1953), the relationships between magnetic properties and microstructure in minerals responsible for the magnetic record in rocks have been an elusive topic. Increasingly we are made aware that submicroscopic texture, ultrafine oxidation products, and precipitates figure significantly in the interpretation of the magnetism. Studies by Davis and Evans (1976), Smith (1979), Schlinger and Veblen (1989), and Price (1980) addressed geometric aspects, such as size and shape, that influence magnetic hardness and stability of remanent magnetism. The role of crystal de-

0003–004X/94/0708–0654$02.00

fects in controlling magnetic properties has also been examined (Jakubovics et al., 1978; Nord and Lawson, 1992; this paper). Although lodestone (natural permanent magnet; see Andrade, 1958) in some ways may be considered a mineralogical curiosity, the factors controlling its highly magnetic nature are of broader significance because they indicate the role of defects and intergrowths in magnetic hardening.

Wasilewski (1977, 1979) noted that the iron ores that possess lodestone properties are composed of either magnetite (type I) or titanomagnetite (type II). All have relatively large values of RI (>0.1) [RI is the ratio of saturation remanence (SIRM) to saturation magnetization (I_S)], indicating microstructural magnetic hardening. The large REM values (≥0.4) [REM is the ratio of natural remanence (NRM) to SIRM] indicate magnetization in a field much larger than the Earth's field. Lightning has been postulated as the mechanism for magnetizing the lodestone (Wilson and Herroun and others, cited in Blackman, 1983). There is currently no other known natural remanence mechanism that could produce the large REM values reported by Wasilewski (1977).

Preliminary thermomagnetic results (Wasilewski, 1977, 1979) suggested that the lodestone sample used in this study was partially oxidized to maghemite (γ-Fe_2O_3). Wasilewski's (1979) measurements suggested that magnetic results were largely the consequence of a microstructure not visible at a magnification of 1000×. Magnetic characteristics of the sample of type I lodestone have been reexamined here in greater detail (especially over the region 100–450 °C), and the results reinterpreted in the light of microstructural information obtained using high-resolution transmission electron microscopy (HRTEM). HRTEM characterization allows detailed correlations among microstructure, mineralogy, and magnetic properties within different thermal regimes. Thus, an understanding of discrete activation of defect microstructure and knowledge of mineral instability are merged to devise a self-consistent model for magnetic behavior of strongly magnetized magnetite and maghemite.

Sample description and experimental methods

The lodestone examined in this study is specimen 99484 from the U.S. National Museum. The sample is from a magnetite deposit near Cedar City, Utah. Electron microprobe, X-ray diffraction (XRD), and magnetic data reported by Wasilewski (1977) indicate that it is composed primarily of magnetite, maghemite, and hematite, with approximately 0.12 wt% Al_2O_3 and 1.2 wt% MgO.

Samples were prepared for transmission electron microscopy both by depositing a suspension of crushed grains on a holey carbon grid and by Ar ion milling. Specimens were examined in a Philips 420ST microscope operated at 120 keV and a Philips CM20UT operated at 200 keV. Selected-area electron diffraction (SAED) patterns and compositional information were used to identify minerals. Analytical electron microscopy (AEM) involved X-ray analyses collected with an EDAX energy-dispersive spectrometer and processed with a PGT System IV analyzer. Most high-resolution images were recorded from crushed grains at magnifications of up to 1 200 000× at close to the Scherzer defocus (−80 nm for the 420ST). High-resolution imaging of ion-milled specimens was extremely difficult because of astigmatism caused by the magnetic field of the sample. Dark-field imaging was used to determine visibility conditions for defects and thus to establish the fault vectors associated with these features.

Additional XRD data were collected on a Scintag automated powder diffractometer using NBS Si 640b as an internal standard. Powder XRD patterns were obtained from unheated samples as well as from those heated to 200–600 °C in thermomagnetic experiments.

Magnetic susceptibility measurements were done using a Barington MS 2 system with an MS2 WFP high-temperature furnace. Magnetic hysteresis measurements and thermomagnetic analyses utilized a PAR model 151 vibrating-sample magnetometer. Remanence measurements were carried out on a 2G superconducting rock magnetometer.

Results

Sample mineralogy

Powder X-ray diffraction patterns from sample 99484 indicate that it is primarily magnetite with some maghemite (~30%) and minor hematite. AEM, convergent-beam electron diffraction (CBED), and powder XRD revealed a patchy distribution of goethite and small, topotactically oriented clinopyroxene (diopside) crystals (Fig. 1; $[111]_{mt} \| [402]_{cpx}$; $\mathbf{b}^*_{cpx} \| [202]^*_{mt}$). Clinopyroxene contains planar defects parallel to (010), possibly chain-width errors (amphibole lamellae).

Magnetic hysteresis, susceptibility, and sample mineral content as functions of temperature

The magnetic susceptibility-temperature curve (Fig. 2a) exhibits a great deal of structure over the temperature range studied. Three distinctive regimes must be correlated with specific mineralogical and microstructural characteristics of the sample over each temperature range. The hysteresis loops measured at points A–F on Figure 2a are shown in Figure 2b. These hysteresis loops were measured at the indicated temperatures.

The first temperature regime (20–280 °C) is associated with an increase in susceptibility and a substantial decrease in coercivity. XRD analyses of samples cooled to room temperature demonstrated the persistence of maghemite and magnetite and no increase in the amount of hematite. Thus, this temperature range precedes the interval over which maghemite is converted to hematite.

Despite the persistence of maghemite, significant irreversible changes take place over the temperature interval 20–280 °C. This is apparent when the magnetic hysteresis loops (measured at room temperature) after heating to 100 (solid loop) and 200 °C (dashed loop) are compared (Fig. 3). The loop at 100 °C is nearly identical to that of the starting material. After heating to 200 °C, the shape

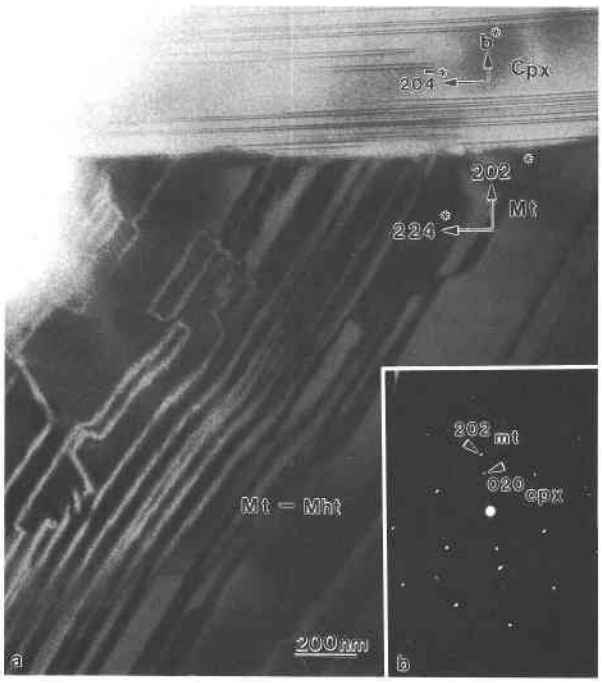

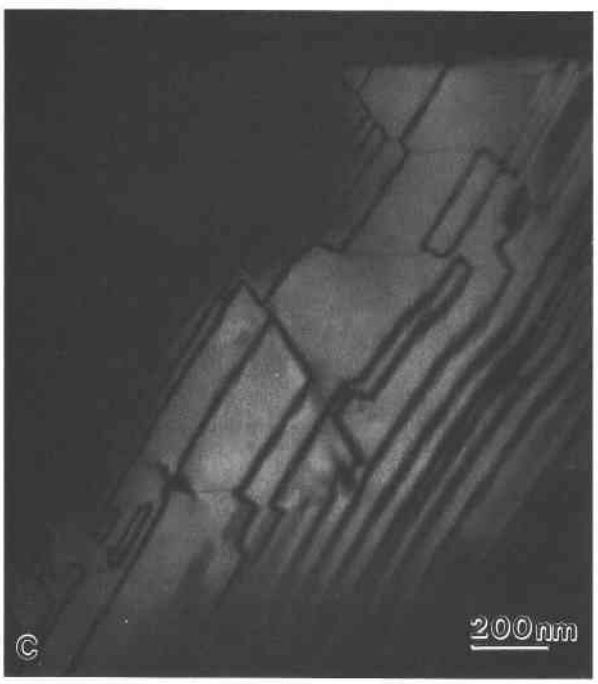

Fig. 1. (**a**) A bright-field transmission electron micrograph showing magnetite (Mt) and maghemite (Mht) that are subdivided by numerous planar features. Planar faults [parallel to (020)] are apparent in the included topotactically oriented clinopyroxene. These may be chain-width errors (i.e., amphibole). (**b**) A selected-area electron diffraction pattern from clinopyroxene [402] and magnetite [111]. Clinopyroxene **b*** is parallel to [202]* of magnetite. (**c**) A dark-field image formed using the $20\bar{2}$ reflection. Two of the three sets of defects are clearly visible.

of the loop changes dramatically, with the field required to close the loop changing from about 0.35 to 0.15 T. The high coercivity exhibited by the loop is lost by 200 °C. These results imply magnetic softening unrelated to any change in the magnetic mineralogy (e.g., the conversion of maghemite to hematite).

The second temperature regime (~280–425 °C), characterized by a precipitous drop in the sample's susceptibility and saturation magnetization (about 20–30% of the value of I_S is lost), corresponds to the destruction of maghemite. XRD analyses showed the replacement of maghemite by hematite.

The third temperature regime (from 425 °C to the Curie point and then back to room temperature) is characterized by the typical susceptibility peak for magnetite near the Curie point (Hopkinson Peak) and gradual increases in the susceptibility and coercivity on cooling. The minerals present in the final sample are magnetite and hematite. The breadth of peaks from magnetite and hematite in powder XRD patterns (compared with massive magnetite) attests to the presence of crystals with sizes in the submicrometer range in the final assemblage of intergrown minerals.

The hysteresis loop after cooling from 600 °C has a different shape compared with that for the unheated sample. The loop for the untreated material (Fig. 2b, loop A) is unusual in that it is of constant width over its entire length. In comparison, the loop for material cooled from its Curie point (Fig. 2b, loop F) has its maximum width near the origin and tapers to closure at higher fields.

Thermal demagnetization of the natural remanent magnetization (NRM)

The thermal demagnetization curves for triplicate specimens are essentially identical (Fig. 4a). About 80% of the NRM is demagnetized by 300 °C, i.e., before the conversion of γ to α-Fe_2O_3. This demagnetization is coincident with the large increase in X_0 (susceptibility) and the corresponding decrease in coercivity. About 15% of the NRM is demagnetized with the conversion of γ- $\rightarrow$ α-Fe_2O_3 between 300 and 400 °C, leaving about 5% of the remanence associated with α-Fe_2O_3 and Fe_3O_4. The inclination of the NRM direction is essentially constant during demagnetization to 550 °C. However, in detail, the declinations cluster for demagnetization to 300 °C and then from 400 to 550 °C.

The points at 600 and 650 °C in the thermal demagnetization curve are essentially antipodal to those of the Fe_3O_4 (Fig. 4b). These points are associated with α-Fe_2O_3 that was produced by the conversion of γ- to α-Fe_2O_3. The reversed NRM of hematite compared with magnetite suggests chemical remagnetization in the laboratory. This effect was not studied in detail.

Remanence and remanence acquisition

The remanent magnetization of sample 99484 is sufficiently intense to justify its classification as a lodestone (Wasilewski, 1977). The ratio of saturation remanence to

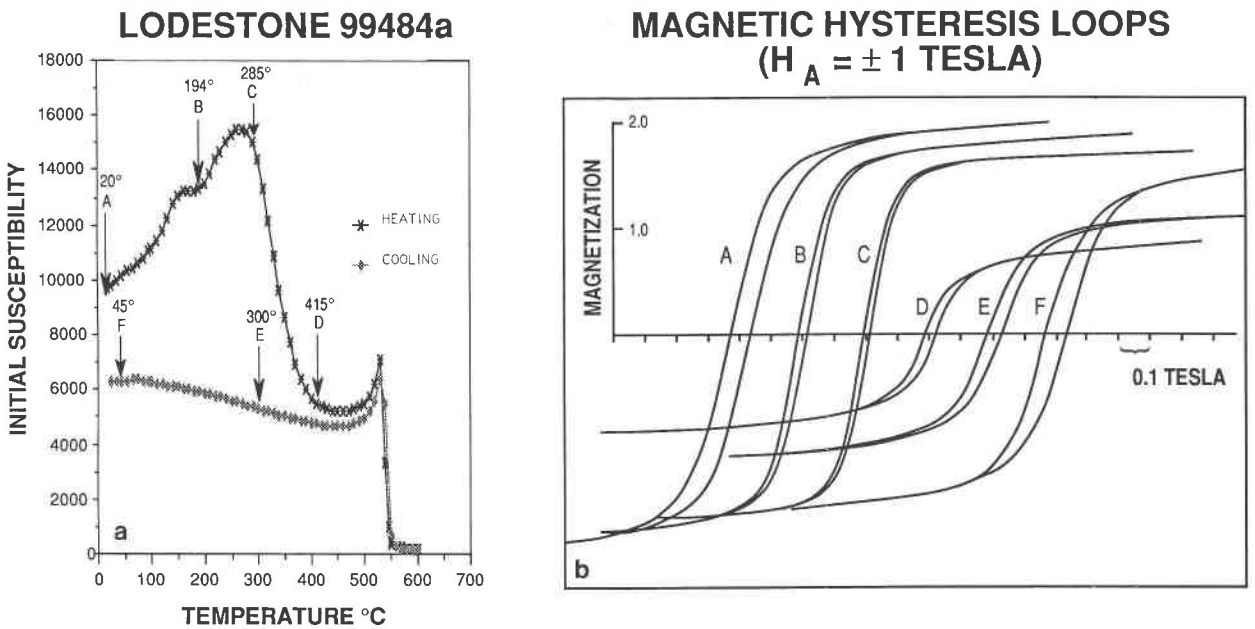

Fig. 2. **(a)** Initial magnetic susceptibility-temperature (X_0-T) heating and cooling curves for sample 99484. The letters A–F at the indicated temperatures correspond to the points at which hysteresis loops shown in **b** were measured. **(b)** Magnetic hysteresis loops labeled A–F correspond to the letters A–F at temperatures indicated on the X_0-T curves in **a**. These loops were measured at the temperature indicated. Loop A is the starting material at room temperature, and F is the room temperature loop for the material after the complete thermal cycle (room temperature to 600 °C to room temperature). $H_A = \pm 1$ T.

saturation magnetization (RI) is in the range 0.18–0.26, compared with values of <0.02 for normal massive magnetite. The REM values (SIRM imparted in a 1-T magnetic field) for seven subsamples range from 0.4 to 0.67. Assessment of all remanent magnetization mechanisms (Nagata, 1961; Stacey and Banerjee, 1974) and comparison with more than a thousand determinations for all types of natural materials studied at the NASA Goddard laboratory (REM values < 0.08) indicate that these REM values are abnormally large for naturally magnetized materials.

Remanence-acquisition curves for sample 99484 (Fig. 5) indicate that magnetic fields in excess of 0.05 T are required to produce the REM values measured for the lodestone. The only way to explain these large REM values is to identify a natural mechanism by which magnetite is exposed to a large field. The hypothesis advanced by Wilson and Herroun, that the magnetization is due to lightning strikes, has been widely considered (Blackman, 1983) and is supported by our data.

The shape of the remanence-acquisition curve (Fig. 5) is nearly identical to that for 1-μm magnetite particles (Thompson, 1986), despite the massive nature of the lodestone samples. Specifically, the field required to achieve one-half of the saturation remanence is about 50 mT. The results of Thompson (1986) for 1-μm magnetite differ from those for sample 99484 in the shape of the hysteresis loop as saturation is approached (the final 15–20% of the remanence is acquired slowly in fields in excess of 0.1 T). The remanence-acquisition curves before heating and after heating to 600 °C are similar, notably because of the overwhelming influence of Fe_3O_4.

Heating to ~285 °C substantially reduces the coercivity (Fig. 2), yet samples cooled from temperatures in excess of those associated with the maghemite to hematite transformation have a high coercivity. Thus, it can be inferred that the microstructure responsible for the acquisition of remanence in samples after heating to 600 °C must differ from that in untreated samples. The final high coercivity must be associated with the size, shape, and distribution of magnetite within the composite of magnetite and hematite.

The levels of saturation remanence observed in sample 99484 require the presence of a microstructure. Without sufficient microstructural hardening, massive magnetite could not be made into a lodestone, even in fields of 1 T. Consequently, we must turn to the microstructural analysis to understand fully the magnetic characteristics of the lodestone.

Microstructural characterization

SAED patterns from extensive areas of iron oxide often show slight splitting of reflections consistent with the presence of both magnetite and maghemite. Some areas, such as the one illustrated in Figure 1, give rise to weak maghemite reflections in SAED patterns (e.g., Fig. 6). These regions are common but sporadically developed.

The most frequently observed arrangement of superstructure reflections involves violation of the face-centering systematic absences, resulting in doubling along the

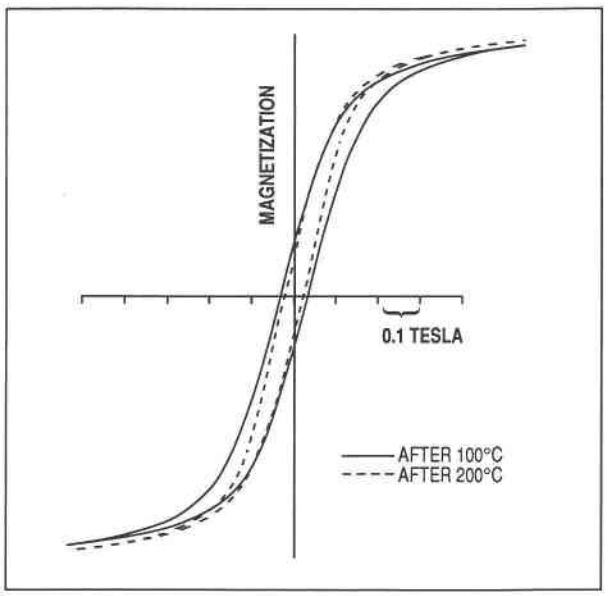

Fig. 3. Magnetic hysteresis loops (measured at room temperature) after heating to 100 (solid loop) and 200 °C (dashed loop) for sample 99484.

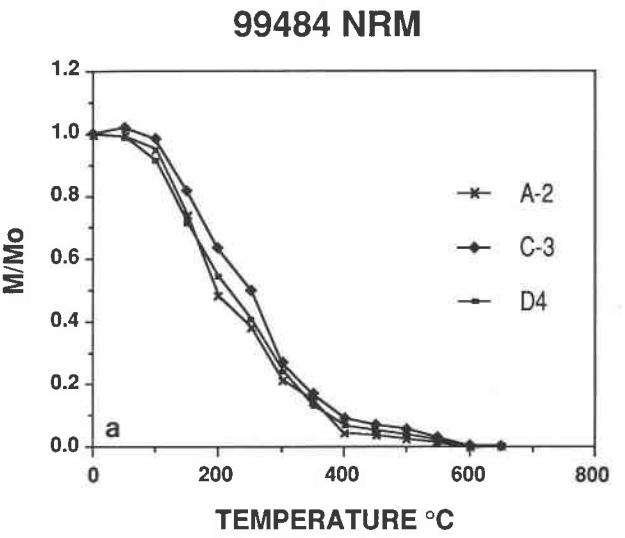

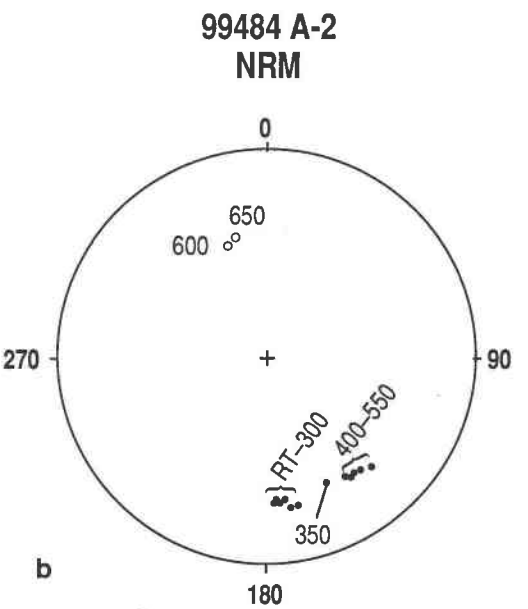

Fig. 4. (a) Stepwise thermal demagnetization curves (ratio of the magnetization, M, to the REM magnetization, M_0, vs. T) for a triplicate subsample array taken from a strip of sample 99484. (b) Behavior of the NRM vector for subsample A-2 [solid circles (−) and open circles (+)]. (RT = room temperature).

⟨202⟩* and ⟨020⟩* directions compared with magnetite (Fig. 6a, 6b). These lattice-centering violations cannot arise from dynamical diffraction (Gjønnes and Moodie, 1965) and are consistent with the $P4_132$ or $P4_332$ space groups previously identified in naturally oxidized magnetite (Smith, 1979). Other arrangements of weak reflections arising from vacancy ordering are evident in some regions. For example, the $4\times$ $(2\bar{4}2)$ repeat (Fig. 6c) that gives rise to a weakly developed periodicity in high-resolution images (Fig. 7) suggests vacancy ordering that doubles the magnetite subcell along one direction. Although an exact identification of the maghemite space group generally could not be made, results are consistent with the formation of a primitive structure exhibiting variable ordering patterns that violate the face-centered lattice of magnetite.

The orientation and distribution of defects

[111] zone. The [111] zone (Fig. 7a) shows three sets of planar features with traces parallel to {220}. Thin areas in this image show doubling along ⟨220⟩*, consistent with the weakly developed superlattice reflections in Figure 6a. The presence of the maghemite superstructure periodicity on either side of the faults indicates that these boundaries do not separate adjacent areas of magnetite and maghemite. The stereographic projection (inset, Fig. 7b) shows the orientation of the other ⟨111⟩ directions, which are the easy directions for magnetization in magnetite and maghemite. High-resolution images show that many of the regions bounded by {202} planes are elongate along $[2\bar{4}2]$ and thus also along ⟨111⟩ (Fig. 7b). At high magnification (Fig. 7c), it is evident that the $(0\bar{2}2)$ and $(2\bar{2}0)$ fringes are offset across the defect parallel to $(20\bar{2})$ planes by approximately half these fringe spacings (seen by sighting along the fringes), equivalent to a displacement of $d_{2\bar{4}2}$. The weakly developed maghemite superstructure is apparent over much of the image.

[121] zone. Figure 8a shows a region bounded by planar features in three orientations. The $(1\bar{1}1)$ fringes appear to

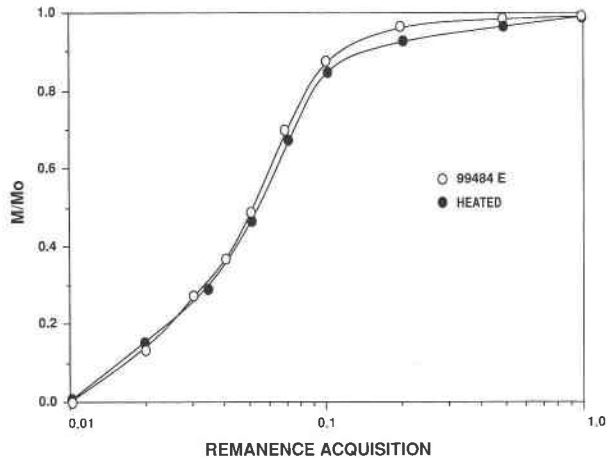

Fig. 5. Remanence-acquisition (ratio of magnetization, M, to REM magnetization, M_0, as a function of the applied field in units of Tesla) curves for 99484. Open circles correspond to the original starting material, and solid circles correspond to the same sample measured after heating to 650 °C.

be offset by approximately $\frac{1}{3}[1\bar{1}1]$ across boundaries marked P_1 and P_2 in Figure 8a. These defects [parallel to $(2\bar{2}0)$ and $(02\bar{2})$] are marked by wide bands of dark contrast (~2 nm) because they are inclined to the electron beam. Offsets of approximately half the $(1\bar{1}1)$ spacing occur along short sections parallel to $(20\bar{2})$ (arrows in Fig. 8a). The $(1\bar{1}1)$ fringes are not offset across the faint planar features parallel to $(20\bar{2})$ (P_3 in Fig. 8a).

[101] zone. Images obtained down [101] show inclined features in two orientations. These features are parallel to the $(2\bar{2}0)$ and $(02\bar{2})$ planes. Figure 9 illustrates that lattice fringes are offset across these defects.

[141] zone. Images down [141] show both vertical and inclined planar features (Fig. 10a). At higher magnifications it is apparent that vertical defects are parallel to $(20\bar{2})$. Defects parallel to $(20\bar{2})$ are interrupted by zigzag segments of inclined features (producing striped contrast) parallel to (220) and (022) (Fig. 10b).

Trace results. Trace results from all the zones reported above are consistent with the presence of defects parallel to the {202} planes (dodecahedral form). Thus, these defects share the known orientation of the domain walls in magnetite (Stacey and Banerjee, 1974).

Fault displacement from HRTEM images

High-resolution images from the [111] zone indicate that the faults are associated with an apparent (projected) displacement equivalent to $d_{2\bar{4}2}$. This is approximately consistent with the projected $\frac{1}{3}[1\bar{1}1]$ displacement indicated by offset of fringes in the [121] zone, and it is in agreement with a [¼0¼] translation within the fault plane (Fig. 11). On the other hand, faults showing no offset of (111) fringes in the [121] zone apparently do not involve a translation.

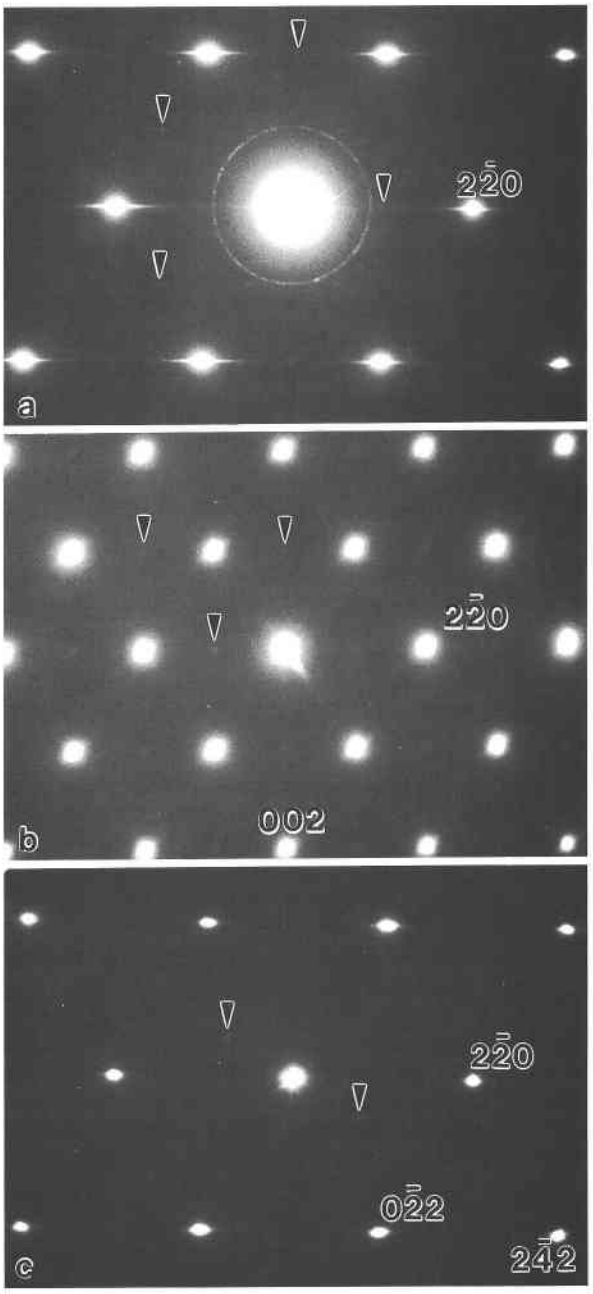

Fig. 6. Selected-area electron diffraction patterns: (**a**) the [111] zone from the area shown in Fig. 1 illustrating weak 110 reflections that should be absent in magnetite; (**b**) the [110] zone illustrating weak 001 and 110 type reflections that should be absent in diffraction patterns from magnetite; (**c**) the [111] zone showing superstructure reflections indicating a 4× multiple of ⟨242⟩ magnetite.

Displacements estimated from HRTEM images were tested by comparing the observed with the expected visibility (Hirsch et al., 1977) using dark-field images formed with different reflections. Contrast from faults is determined by the phase change $\alpha = 2\pi\mathbf{g}\cdot\mathbf{R}$ across the fault (**g**

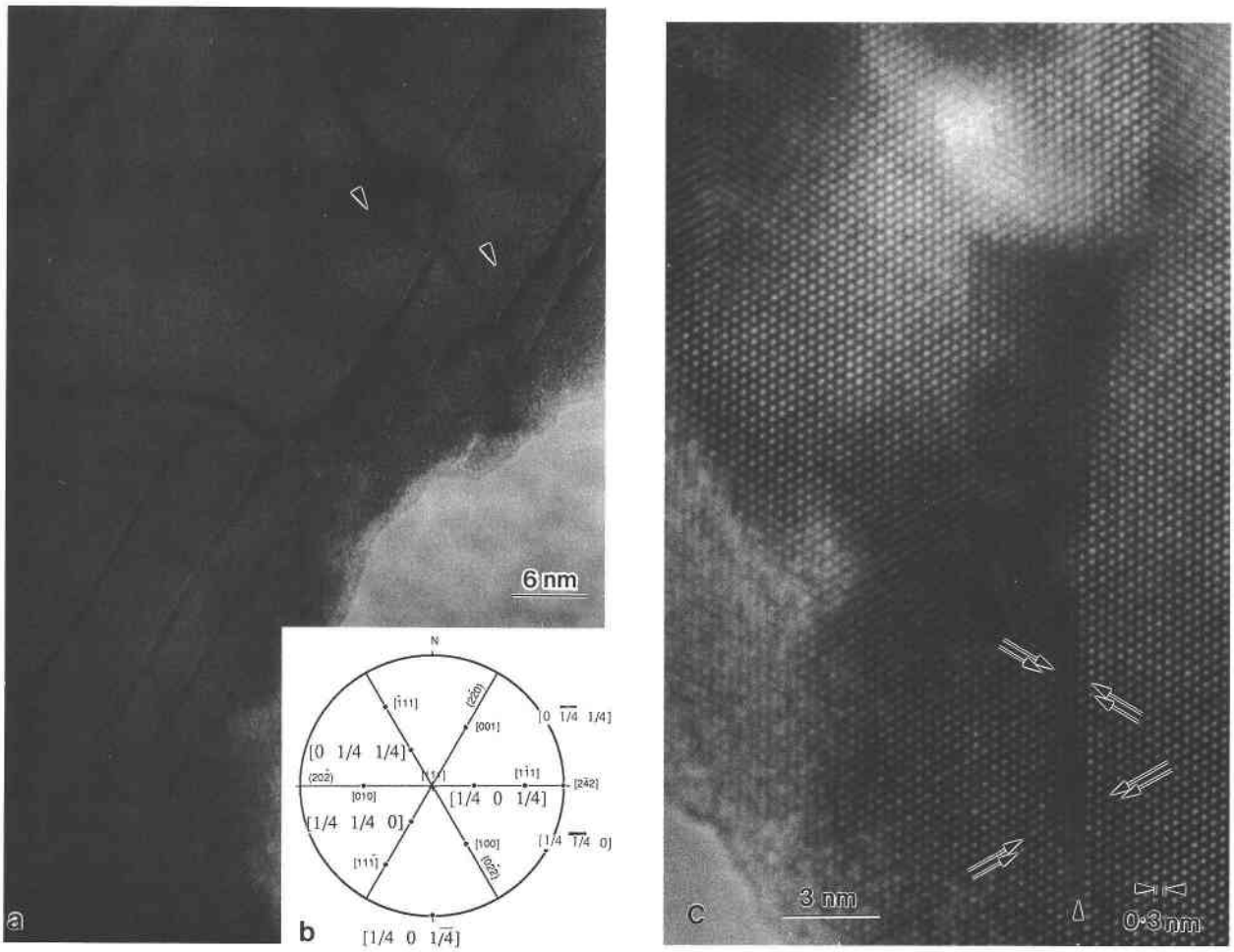

Fig. 7. (**a**) Transmission electron micrograph of the [111] zone illustrating three sets of planar features with traces parallel to {110}. Areas showing doubling are indicated by arrows. (**b**) Stereographic projection for the [111] zone. (**c**) High-resolution image showing that $(0\bar{2}2)$ and $(2\bar{2}0)$ fringes are offset by the defect parallel to the $(20\bar{2})$ planes.

= reciprocal lattice vector; **R** = fault vector). For example, when $\alpha = 0, 2\pi$ ($\mathbf{g}\cdot\mathbf{R} = 0 \pm 1, \pm 2, \ldots \pm n$, where n is an integer), there is no contrast. We evaluated the displacement vectors associated with many faults. Examples from two areas are given below.

Displacement vector analysis by dark-field imaging

[111] zone. A dark-field image formed using the $20\bar{2}$ reflection for the area in Figure 1a is shown in Figure 1c. Comparing these images shows that faults in two orientations parallel to the $(0\bar{2}2)$ and $(2\bar{2}0)$ planes are highly visible, whereas the faults parallel to the $(20\bar{2})$ planes are effectively invisible. These observations can be analyzed using the visibility criteria noted above; the results are shown in Table 1.

[121] zone. Dark-field images of an area were formed using the $40\bar{4}$ reflection (Fig. 12a), the $31\bar{1}$ reflection (Fig. 12b), and the $62\bar{8}$ reflection (Fig. 12c). The bright-field image obtained with the beam parallel to [121] (Fig. 12d) illustrates inclined defects [parallel to the $(2\bar{2}0)$ and $(0\bar{2}2)$ planes] that show fringe offsets and vertical defects parallel to the $(20\bar{2})$ planes that show no fringe offset. In Figure 11a and 11b, the faults that offset the (111) fringes are effectively invisible. In Figure 12a the defects parallel to the $(20\bar{2})$ planes are somewhat visible, and in Figure 12b they are nearly invisible. In Figure 12c the $(20\bar{2})$ and $(0\bar{2}2)$ defects are clearly visible, whereas those parallel to $(2\bar{2}0)$ are invisible. Results are analyzed in Table 1.

Observations indicate that faults for which a translation was found are in contrast under the conditions expected for a displacement vector with a length of 0.297 nm (equal to the 220 interplanar spacing) contained within the fault plane, and thus they are stacking faults with translations of the type [¼¼0]. The stacking faults preserve the arrangement of O atoms. The boundary structure is illustrated in Figure 13a. Faults that do not offset the (111) fringes in the [121] zone cannot have a ⟨¼¼0⟩

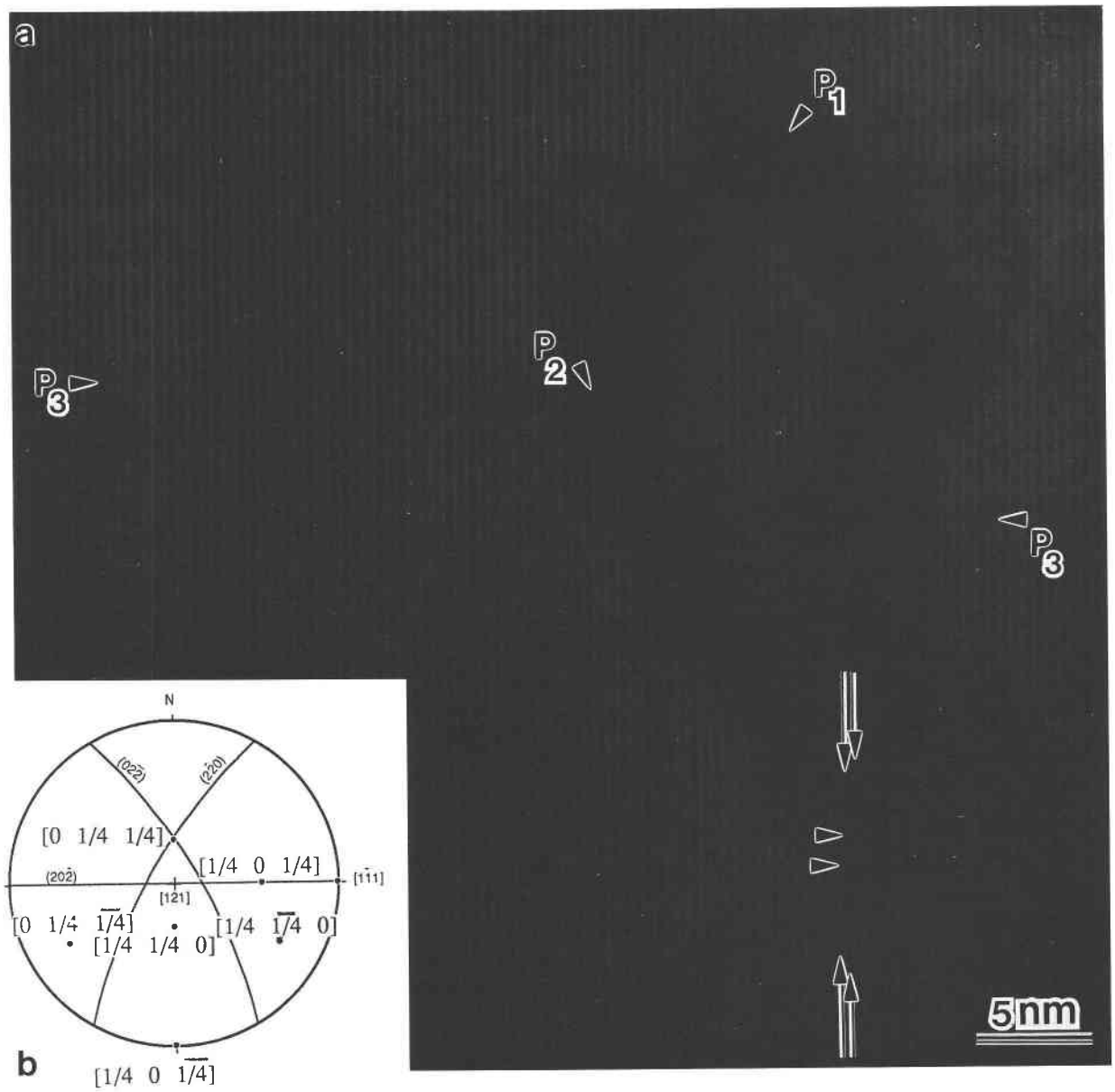

Fig. 8. (**a**) Transmission electron micrograph of the [121] zone showing the traces of planar features in three orientations (P_1, P_2, P_3). The ($1\bar{1}1$) fringes are offset by the two sets of inclined defects (P_1, P_2). (**b**) Stereographic projection for the [121] zone.

displacement and show contrast that is inconsistent with a translational displacement of this type.

Contrast alternation in dark-field images. Figure 14 is a dark-field image (242 reflection) from an area exhibiting a well-developed maghemite superstructure. Two of the three sets of faults are visible in this image. Effective invisibility was achieved under dark-field conditions using the $4\bar{4}0$ reflection, suggesting that these boundaries also involve a [¼¼0]-type translation. The image shows alternation of contrast associated with the fault boundaries. It is difficult to attribute contrast alternation to different magnitudes for the 242 structure factors in alternate regions (e.g., if the faults separate regions of left and right variants of maghemite), as these differences will be small. Contrast alternation may in part reflect strain associated with the defects (G. Nord, 1993 written communication).

Microstructure of the sample heated to 200 °C

The sample heated to 200 °C in the susceptibility-temperature experiments (Fig. 2a) was characterized by XRD and its microstructure examined by TEM. Most of the fragments composed of maghemite and magnetite appeared to be devoid of stacking faults, although occasional dislocations were present. Some small regions exhib-

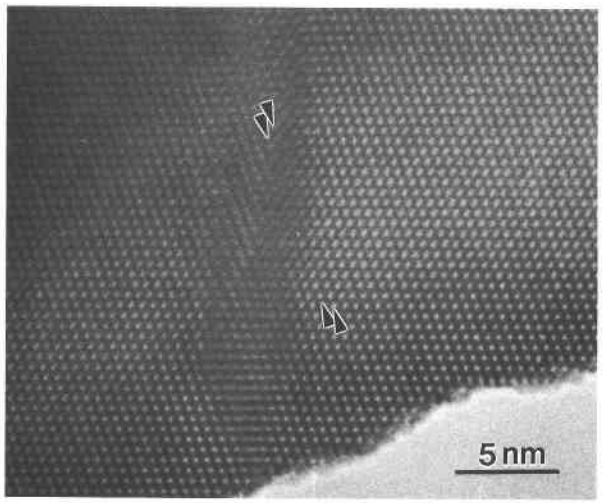

Fig. 9. Image down [101] illustrating that lattice fringes are offset across an inclined defect [defect parallel to (2$\bar{2}$0)].

ited the characteristic stacking-fault microstructure described in the unheated lodestone. The microstructure present within clinopyroxene lamellae was unchanged.

Discussion

The very high REM and saturation remanence values, the susceptibility-temperature behavior, thermal demagnetization results, and remanence-acquisition characteristics all indicate that the distinctive magnetic properties of lodestone sample 99484 must be explained by consideration of the minerals and their microstructures. Furthermore, understanding of the thermal stability of the magnetic properties requires characterization of changes in mineral content and microstructure with temperature.

Table 1. Determination of displacement vectors for faults based on visibility criteria for **g** = 20$\bar{2}$, 40$\bar{4}$, 31$\bar{1}$, and 62$\bar{8}$

Fault plane	**g**·**R**	$\alpha = 2\pi$**g**·**R**	Visibility	
			Predicted	Observed
(2$\bar{2}$0)	(20$\bar{2}$)·[¼¼0]	$+\pi$	visible	visible
(0$\bar{2}$2)	(20$\bar{2}$)·[0¼¼]	$-\pi$	visible	visible
(202)	(20$\bar{2}$)·[¼0¼]	0	invisible	invisible
(2$\bar{2}$0)	(40$\bar{4}$)·[¼¼0]	2π	invisible	invisible
(0$\bar{2}$2)	(40$\bar{4}$)·[0¼¼]	-2π	invisible	invisible
(202)	(40$\bar{4}$)·[¼0¼]	0	invisible	visible
(2$\bar{2}$0)	(31$\bar{1}$)·[¼¼0]	2π	invisible	invisible
(0$\bar{2}$2)	(31$\bar{1}$)·[0¼¼]	0	invisible	invisible
(202)	(31$\bar{1}$)·[¼0¼]	π	visible	invisible
(2$\bar{2}$0)	(62$\bar{8}$)·[¼¼0]	4π	invisible	invisible
(0$\bar{2}$2)	(62$\bar{8}$)·[0¼¼]	-3π	visible	visible
(202)	(62$\bar{8}$)·[¼0¼]	$-\pi$	visible	visible

High-resolution imaging, electron diffraction, trace analysis, and fault vector analysis have been used to analyze the distribution, orientation, and displacement vectors of defects in the lodestone sample. The results indicate that the sample is subdivided into domains that are typically only a few tens of nanometers wide by planar faults, many of which offset the magnetite substructure. Images such as Figure 7c suggest that the fault width is small (<0.6-nm wide) and that a second phase several unit cells wide is not developed along these features.

The presence of a weakly developed superstructure indicates that some of the magnetite in the lodestone specimen has been oxidized to form maghemite. This reaction can be written $3Fe_3O_4 + 0.75O_2 + 3H^+ \rightarrow 4\gamma\text{-}Fe_2O_3 + Fe^{3+} + 1.5H_2O$. Wasilewski (1977, 1979) suggested that the sample was composed of finely intergrown, alternating lamellae of maghemite and magnetite. However, the presence of the maghemite superstructure on

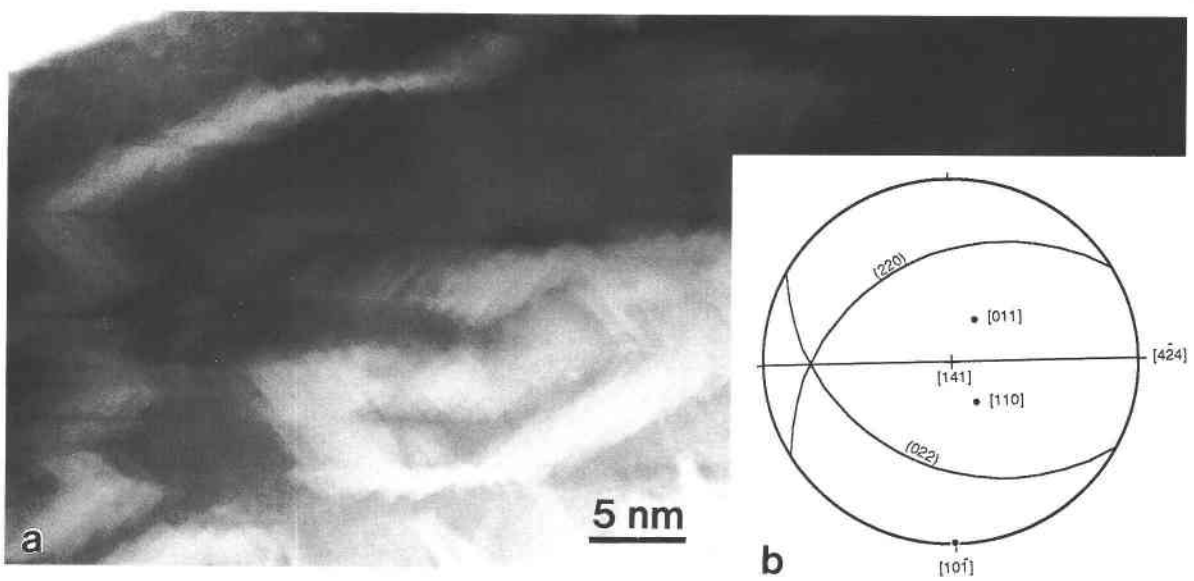

Fig. 10. (a) A [141]-zone image showing contrast associated with inclined defects; (b) a stereographic projection for the [141] zone.

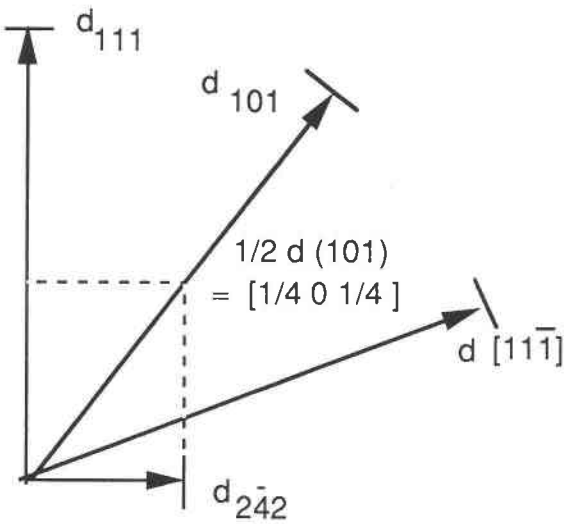

Fig. 11. Diagram illustrating that projected translations are consistent with a [¼0¼] Burgers vector.

either side of boundaries indicates that stacking faults commonly separate adjacent regions of maghemite and not magnetite from maghemite.

Maghemite microstructures

Maghemite exhibits superstructure reflections that are generally consistent with the enantiomorphic space groups $P4_132$ and $P4_332$ reported for maghemite by Smith (1979). Smith (1979) discussed seven boundaries with ⟨½½0⟩ translations that are expected when magnetite converts to maghemite with these structures. In our samples, planar features showing no offset of the magnetite substructure (Fig. 8a, P_3) might be boundaries between adjacent maghemite domains.

Microstructures involving the magnetite subcell

Offsets for faults parallel to {101} were determined by HRTEM imaging and dark-field experiments involving subcell reflections. Results show that most boundaries in maghemite and magnetite can be described as stacking faults with a ⟨¼¼0⟩ displacement. Because these boundaries offset the magnetite substructure, they cannot have formed simply as the result of vacancy creation during oxidation.

Hornstra (1960) considered defects in spinel from a theoretical perspective and suggested that the most likely slip plane is {111}. However, Lewis (1966) showed experimentally that the principal glide system for nonstoichiometric spinels was of the type {110}⟨110⟩. Lewis re-

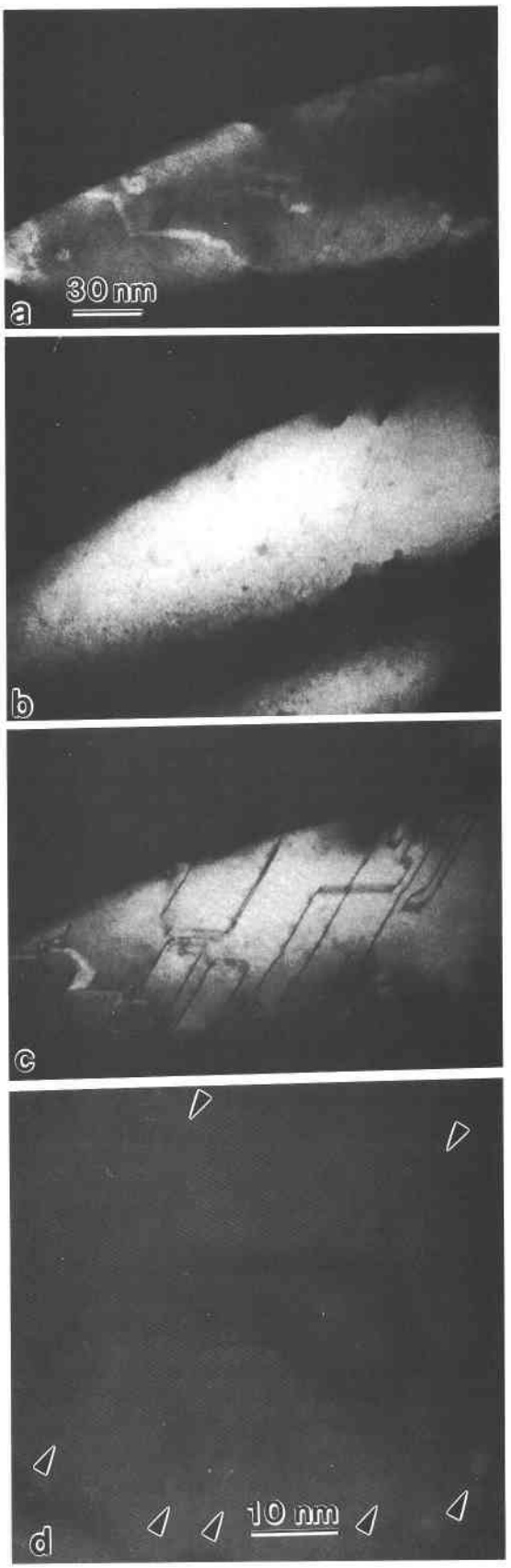

→

Fig. 12. Dark-field images formed using (**a**) the 40$\bar{4}$ reflection, (**b**) the 3$\bar{1}$1 reflection, and (**c**) the 62$\bar{8}$ reflection. (**d**) Bright-field [121]-zone image for the area shown in **a**, **b**, and **c**. The arrows indicate planar defects that do not offset the (1$\bar{1}$1) fringes.

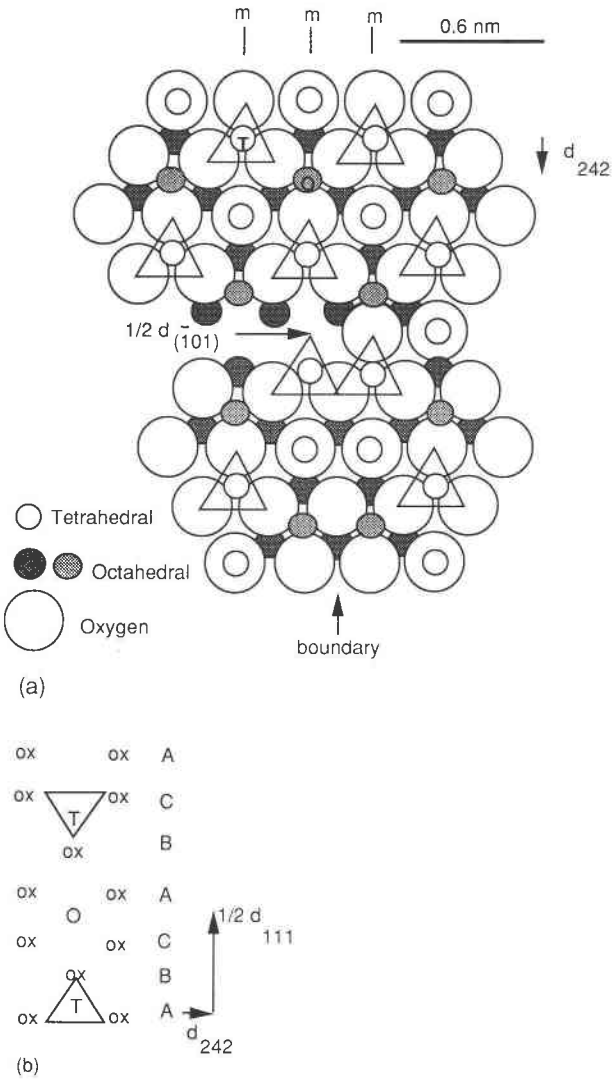

Fig. 13. (**a**) Diagram down [111] illustrating the distribution of cations above and below a single O layer in magnetite. The lower part of the diagram results from a translation of ½ (101) = [−¼0¼] perpendicular to the boundary. (**b**) An identical displacement (relating T and O in **a**) is achieved if a translation of d_{242} is followed by a translation of $\frac{1}{2}d_{111}$.

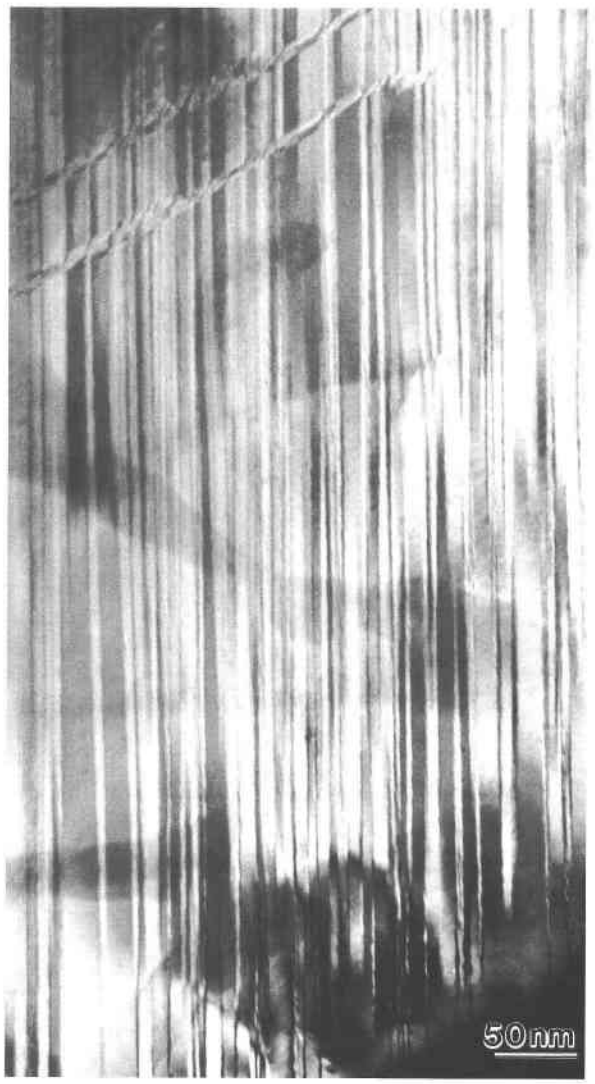

Fig. 14. Dark-field image formed using the 242 reflection for an area showing a well-developed maghemite superstructure (diffraction pattern shown in Fig. 6b). Alternating regions with dark and light contrast separated by defects may be due either to strain contrast or to maghemite in twin-related orientations.

ported that deformation-induced Burgers vectors had magnitudes of ½⟨110⟩. These were commonly dissociated into two partial dislocations with ¼⟨110⟩ Burgers vectors, separated by a stacking fault. The separation of the partial dislocations increased with increasing degree of nonstoichiometry. Lewis (1966) considered the structure of these defects and noted that cation polyhedra must share some faces in the fault plane, unlike in the unfaulted bulk structure. By analogy with the work of Lewis (1966), we suggest that stacking faults described in our work may be the result of dissociation of deformation-induced dislocations.

Stacking faults in our samples are developed preferentially along one of the sets of {110} planes in magnetite, producing needle-shaped domains. If the faults formed by deformation, we suggest that the event may have been highly directional, favoring one of a set of otherwise symmetrically equivalent slip systems.

Combined microstructures

Some areas containing stacking faults that offset the magnetite substructure also display characteristics that arise from maghemitization. Consequently, the boundaries separating maghemite domains and showing ⟨¼¼0⟩-type offset of the subcell might also have a ⟨½½0⟩-type offset of the superstructure (as reported by Smith, 1979). In our samples, the superstructure was not sufficiently

well developed to show this phenomenon clearly. The presence of face-sharing tetrahedral and octahedral sites along the fault surface might promote nucleation of adjacent domains of maghemite with enantiomorphic cation distribution patterns within the undisturbed O framework. This vacancy distribution pattern could minimize the stacking fault energy.

In summary, the distinctive microstructures of the lodestone specimen are apparently the result of both structural faulting of magnetite and its oxidation to maghemite. Stacking faults might have provided nucleation sites (and possibly rapid-diffusion pathways) for maghemite growth, or stacking faults might have developed within maghemitized magnetite.

Magnetic properties and their relation to microstructure

In combination, the magnetics experiments (Figs. 2–5) and microstructural analysis provided explanations for the distinctive properties of lodestone sample 99484 and the changes in these properties with temperature.

Untreated samples. Lodestone carries a sufficiently large natural remanence to indicate exposure to a magnetization event of a magnitude far in excess of that associated with the Earth's magnetic field. The REM values (0.4–0.67 for seven subsamples) are much larger than those measured for most naturally magnetized materials. We support the view that the high REM values imply an NRM that is composed mostly of a lightning-induced remanence.

Remanence-acquisition and coercivity data indicate the importance of microstructure in establishing the magnetic properties of the lodestone. We attribute the distinctively high coercivity to the presence of planar defects in magnetite and maghemite. The arrangement of stacking faults ({101} or dodecahedral form) shares the orientations of normal magnetic domain walls in magnetite (Stacey and Banerjee, 1974). Most of the high coercivity of the sample can almost certainly be associated with the presence of these faults, which serve as (or pin) magnetic domain boundaries (e.g., rotation of magnetic vectors would require nucleation of new domain walls or motion of the faults).

This role of stacking faults in controlling the coercivity is supported by the work of Jakubovics et al. (1978), who reported that magnetite formed from hematite in the electron microscope contained faults on {110} planes with vectors of ¼⟨110⟩. They used Lorentz microscopy to show that stacking faults strongly influenced the magnetic domain structure, and they applied a simplified model to show that stacking faults will be low-energy sites for magnetic domain walls. By analogy with their work, most of the natural remanence in our samples is probably associated with these abundant structural defects.

The shape of the hysteresis loop (constant width until near saturation) for unheated sample 99484 is distinctive compared with that of finely subdivided magnetite (Thompson, 1986). We suggest that the loop shape for lodestone reflects a mixture of very hard (defect regions) with relatively soft (defect-free) material, causing the loop to be constricted as it approaches the origin.

Small, topotactically oriented diopside crystals are also common in the sample. Their boundaries are parallel to {202} fault planes in maghemite (Fig. 1). Consequently, these features subdivide the sample in the same way as the faults and, thus, also may contribute to magnetic hardening.

Most of the images indicate that the structural domains, and thus possibly the magnetic domains, are needle-shaped, with elongation along one of the [111] directions. The shape anisotropy parallel to an easy direction for magnetization (Stacey and Banerjee, 1974) may enhance the ability of the crystals to acquire a unidirectional alignment.

Samples heated to ~285 °C. Hysteresis loops decreased in width considerably throughout the 20–285 °C temperature range (A–C in Fig. 2b), indicating very substantial magnetic softening. Between room temperature and 100 °C, the increase in susceptibility (X_0) was essentially reversible, and the magnetic hysteresis loop data indicate that little of the hard magnetization (ascribed to stacking faults) was altered.

Between 100 and 200 °C, the coercivity was diminished (see Fig. 2), and magnetic susceptibility increased steeply (100–150 °C). The susceptibility remained essentially unchanged between 150 and 200 °C. No evidence for any appreciable conversion of γ- to α-Fe_2O_3 was detected after heating to 200 °C, but the stacking fault density was significantly reduced (some apparently unmodified areas remained).

Heating from 200 to about 280 °C was accompanied by a continuous increase in X_0 and a decrease in coercivity. These changes are unrelated to the conversion of γ- to α-Fe_2O_3 (which occurs at higher temperature) and appear to be directly associated with the elimination of stacking faults. The plateau in the X_0 curve (150–200 °C) is interpreted to indicate a thermal range where some stacking fault configurations are stable, possibly indicating a two-stage process for the elimination of these features (the first between 100 and 150 °C and the second between 200 and 280 °C). Elimination of stacking faults may involve recombination of partial dislocations and reorganization of dislocations to grain boundaries.

The susceptibility increase over the interval 20–280 °C is attributed to the increase in size of magnetic phase volumes (topotactic Fe_3O_4–γ-Fe_2O_3 regions) due to elimination of the faults. The coercivities for the starting material (22–29 mT) were reduced to 15–20 mT after heating to 300 °C (measured at room temperature). Measured at 300 °C, the coercivities were 5–6 mT. These coercivities were larger than expected for coarse multidomain magnetite, even with hematite lamellae introduced by moderate amounts of normal oxidation (<5 mT). Thus, the Fe_3O_4–γ-Fe_2O_3 regions remain magnetically hard in the absence of faults. The bounding regions (and any reconstructed defect microstructure) are possible sources of this hardness.

Thermal demagnetization results (Fig. 4) reveal that the period of greatest loss of natural remanence corresponds with the 20–285 °C temperature interval and, thus, with the dramatic decrease in coercivity. This further supports the correlations among coercivity, remanence, and stacking faults, as well as the view that pinning of magnetic domain walls to stacking faults gives lodestone its high natural remanence.

300–600 °C. X-ray powder diffraction patterns confirmed that heating to temperatures between ~300 and 425 °C results in the conversion of maghemite to hematite. The γ- $\rightarrow$ α-Fe_2O_3 transformation has a clear magnetic signature. The susceptibility and saturation magnetization decrease rapidly and almost all remaining NRM (~20%) is lost.

The coercivity of the hematite-bearing samples was considerably larger than that of samples heated to just below the maghemite-hematite transformation. The final coercivity of the sample cooled from 600 °C was similar to that of the unheated sample. This implies that a secondary microstructure had been created by the growth of hematite. Furthermore, the remanence-acquisition curve for the sample after heating to ~600 °C was almost identical to that of the unheated sample. The coincidence of the initial and final coercivity values is probably fortuitous in this case and might be attributed to the specifics of the shape and distribution of reaction products, as well as the strong shape anisotropy of the remaining magnetite. In a different magnetite lodestone (97425 of Wasilewski, 1979), about 50% of the coercivity was recovered after the inferred maghemite $\rightarrow$ hematite conversion.

The apparently small crystal size of both magnetite and hematite in the demagnetized material (as indicated by peak broadening in XRD traces) may indicate that the final microstructure is composed of magnetite and hematite intergrown on a sufficiently fine scale to induce magnetic hardening. The hysteresis loop for this material (Fig. 2b, curve F) is similar to that of magnetite without an admixed, magnetically very hard component (stacking fault regions).

Both the magnetic measurements and the microstructure place constraints on the timing of events producing lodestone. The high REM value requires that structural faulting either predated or formed simultaneously with magnetization. The anisotropic distribution of faults (and the absence of similar features in magnetite from other rocks previously examined by the authors) suggests that the events occurred simultaneously. Thus, stacking faults may be attributable to shock and the NRM to the magnetic field associated with a lightning discharge.

Conflicting views have been offered as to the extent to which CRM preserves the NRM (e.g., Marshall and Cox, 1971; Johnson and Merrill, 1972, 1973; Prévot et al., 1981; Smith and Banerjee, 1986; Raymond and LaBrecque, 1987; Nishitani and Kono, 1989). In our samples, data suggest that destruction of maghemite is accompanied by migration of the net magnetization vector, implying that the component carried by magnetite is slightly skewed from that carried by maghemite. The hematite with reversed magnetization acquired its remanence between 300 and 450 °C during the γ- $\rightarrow$ α-Fe_2O_3 conversion in the presence of magnetite. The magnetization residing in Fe_3O_4 is so intense, even at 550 °C, that only at 600 °C when Fe_3O_4 is demagnetized completely do we see the α-Fe_2O_3 magnetization.

General implications and conclusions

The results of this study emphasize that microstructures can greatly influence mineral magnetic properties. The correspondence of stacking fault and magnetic-domain wall orientations and the elongation of fault-bounded regions along the easy direction for magnetization suggest that it is the presence of defects (and, we infer, lightning strikes) that make this sample magnetically distinct from normal, multidomain magnetite.

Defects may have been introduced by an as yet unidentified process before magnetization. However, we consider it likely that structural faulting occurred simultaneously with the acquisition of the high NRM. We support the view that lightning discharge was responsible both for the magnetization and the development of the stacking faults (probably through dislocation dissociation). The timing of maghemite formation is unclear. However, thermal demagnetization data suggest that the NRM carried by the maghemite is skewed relative to that carried by magnetite.

The geometric configuration and thermal dependence of γ-Fe_3O_4 were originally proposed to explain the magnetic behavior of sample 99484 (Wasilewski, 1979). Interfacial behavior associated with epitactic intergrowths of magnetite and maghemite was considered responsible for the magnetic hardness of the starting material. It was hypothesized that the destruction of maghemite in intergrowths of magnetite and maghemite resulted in elongate regions of magnetite separated by hematite, and this was considered the source of magnetic hardness after heat treatment. Microstructural evidence reported above identifies stacking faults as immobile sites for domain walls and provides a firm basis for the explanation of the thermomagnetic behavior of the sample composed of magnetite and maghemite. At temperatures below the maghemite-hematite transformation the material is magnetically softened as structural defects are eliminated. However, the magnetic hardness of the sample after final heat treatment is related to the destruction of maghemite. Results clarify the role of maghemite and indicate that most of the significant magnetic behavior, including remanence demagnetization, can be related to the temperature response of stacking faults.

Recognition of microstructures (often with a large shape aspect) capable of pinning magnetic domain walls or retarding wall motion (e.g., ultrafine oxidation products, precipitates, and extended defects) and characterization of mineralogic and microstructural changes with heating allow us to refine our interpretations of magnetic data. The structure of the X_0-T curve and associated magnetic

hysteresis and thermal demagnetization records are explained by TEM and XRD data on the size and shape of magnetic phases and the thermal regimes where stacking faults and maghemite are stable. Results suggest that the fine structure of the X_0-T curve can be used to localize thermal regimes in which defect activation and phase transformation (e.g., γ- $\rightarrow$ α-Fe_2O_3) are important, providing insights into the thermal stability of features shown to preserve remanence. This might be important for the interpretation of paleomagnetic records, illustrating, for example, how magnetic records could be modified during low-grade thermal metamorphism.

The rock magnetism literature contains numerous examples of anomalous susceptibility-temperature curves and studies that contrast thermal and alternating-field demagnetization results from the same samples. The detailed explanation for some of these results might involve microstructures and metastable phases that could be characterized by electron microscopy. For example, Nord and Lawson (1992) presented evidence that compositionally distinct twin-domain boundaries arising from the order-disorder transition in certain ilmenite-hematite series phases have a dramatic effect on magnetic properties. Our data further demonstrate the importance of microstructures, in this case stacking faults, in magnetic hardening and in pinning remanent magnetization. Only through an understanding of its microstructures can we explain how a piece of magnetite the size of a book can exhibit the characteristics of a pseudosingle domain.

Acknowledgments

Special thanks are expressed to Charles Schlinger, Özden Özdemir, Paul Kelso, and David Dunlop for useful suggestions and very helpful discussions of the observations reported here. Gordon Nord provided an exceptionally astute review of this manuscript. An anonymous reviewer is also thanked for constructive suggestions. Robert Fudali of the U.S. National Museum provided the lodestone samples. Electron microscopy research was supported by a Mineralogical Society of America grant and NSF grant EAR-9207041 to J.F.B. and NSF grant EAR-8903630 to D.R.V. Magnetics research was supported by the NASA Geology Program.

References cited

Andrade, E.N. (1958) The early history of the permanent magnet. Endeavor, 17, 22–30.

Blackman, M. (1983) The lodestone: A survey of the history and physics. Contemporary Physics, 24, 319–331.

Davis, P.M., and Evans, M.E. (1976) Interacting single-domain properties of magnetite intergrowths. Journal of Geophysical Research, 81, 989–994.

Gjønnes, J., and Moodie, A.F. (1965) Extinction conditions in the dynamic theory of electron diffraction. Acta Crystallographica, 19, 65–67.

Graham, J.W. (1953) Changes of ferromagnetic minerals and their bearing on ferromagnetic properties of rocks. Journal of Geophysical Research, 58, 243–260.

Hirsch, P., Howie, A., Nicholson, R.B., Pashley, D.W., and Whelan, M.J. (1977) Electron microscopy of thin crystals (2nd edition), 563 p. Krieger, Malabar, Florida.

Hornstra, J. (1960) Dislocations, stacking faults, and twins in the spinel structure. Physics and Chemistry of Solids, 15, 311–323.

Jakubovics, J.P., Lapworth, A.J., and Jolly, T.W. (1978) Electron microscope studies of ferromagnetic ordered structures. Journal of Applied Physics, 49, 2002–2006.

Johnson, H.P., and Merrill, R.T. (1972) Magnetic and mineralogical changes associated with low-temperature oxidation of magnetite. Journal of Geophysical Research, 77, 334–341.

——— (1973) Low-temperature oxidation of titanomagnetite and the implications for paleomagnetism. Journal of Geophysical Research, 78, 4938–4949.

Lewis, M.H. (1966) Defects in spinel grown by the Verneuil process. Philosophical Magazine, 14, 1003–1018.

Marshall, M., and Cox, A. (1971) Effect of oxidation on the natural remanent magnetization of titanomagnetites in suboceanic basalts. Nature, 230, 28–31.

Nagata, T. (1961) Rock magnetism (revised edition), 350 p. Maruzen, Tokyo.

Nishitani, T., and Kono, M. (1989) Effect of low-temperature oxidation on the remanence properties of titanomagnetites. Journal of Geomagnetism and Geoelectricity, 41, 19–38.

Nord, G.L., Jr., and Lawson, C.A. (1992) Magnetic properties of ilmenite$_{30}$-hematite$_{70}$: Effect of transformation induced twin boundaries. Journal of Geophysical Research, 97B, 10897–10910.

Prévot, M., Lecaille, A., and Mankinen, E.A. (1981) Magnetic effects of maghemitization of oceanic crust. Journal of Geophysical Research, 86, 4009–4020.

Price, G.D. (1980) Exsolution microstructures and their magnetic significance. Physics of the Earth and Planetary Interiors, 23, 2–12.

Raymond, C.A., and LaBrecque, J.L. (1987) Magnetization of the oceanic crust: Thermoremanent magnetization or chemical remanent magnetization? Journal of Geophysical Research, 92, 8007–8088.

Schlinger, C.M., and Veblen, D.R. (1989) Magnetism and transmission electron microscopy of Fe-Ti oxides and pyroxenes in a granulite from Lofoten, Norway. Journal of Geophysical Research, 94, 14009–14026.

Smith, G.M., and Banerjee, S.K. (1986) Magnetic structure of the upper kilometer of the marine crust at Deep Sea Drilling Project Hole 504B, Eastern Pacific Ocean. Journal of Geophysical Research, B91, 10337–10354.

Smith, P.P.K. (1979) The observation of enantiomorphous domains in natural maghemite. Contributions to Mineralogy and Petrology, 69, 249–254.

Stacey, F.D., and Banerjee, S.K. (1974) The principles of rock magnetism: Developments in solid earth geophysics, vol. 5, 195 p. Elsevier Scientific, New York.

Thompson, R. (1986) Modelling magnetization data using SIMPLEX. Physics of the Earth and Planetary Interiors, 42, 113–127.

Uyeda, N. (1958) Thermoremanent magnetization as a medium of paleomagnetism with special reference to reverse thermoremanent magnetization. Japanese Journal of Geophysics, 2, 1–23.

Wasilewski, P.J. (1977) Magnetic and microstructural properties of some lodestones. Physics of the Earth and Planetary Interiors, 15, 349–362.

——— (1979) Lodestone: Explanation for magnetic properties and characterization of the source of magnetic hardening. Journal of Applied Physics, 50, 2428–2430.

Manuscript received September 4, 1992
Manuscript accepted March 4, 1994